High-sensitivity strain sensor based on in-fiber improved Fabry–Perot interferometer

Shen Liu, Yiping Wang,* Changrui Liao, Guanjun Wang, Zhengyong Li, Qiao Wang, Jiangtao Zhou, Kaiming Yang, Xiaoyong Zhong, Jing Zhao, and Jian Tang

Key Laboratory of Optoelectronic Devices and Systems of Ministry of Education and Guangdong Province, Shenzhen University, Shenzhen 518060, China

**Corresponding author: ypwang@szu.edu.cn*

Received January 21, 2014; revised February 27, 2014; accepted February 27, 2014; posted March 3, 2014 (Doc. ID 205105); published March 31, 2014

We demonstrated a high-sensitivity strain sensor based on an in-fiber Fabry–Perot interferometer (FPI) with an air cavity, which was created by splicing together two sections of standard single-mode fibers. The sensitivity of this strain sensor was enhanced to 6.0 pm/με by improving the cavity length of the FPI by means of repeating arc discharges for reshaping the air cavity. Moreover, such a strain sensor has a very low temperature sensitivity of 1.1 pm/°C, which reduces the cross sensitivity between tensile strain and temperature. © 2014 Optical Society of America

OCIS codes: (120.2230) Fabry-Perot; (060.2370) Fiber optics sensors.
http://dx.doi.org/10.1364/OL.39.002121

Fiber-optic Fabry–Perot interferometers (FPIs) have proved to be useful in the measurements of various physical, chemical, and biological parameters because of the advantage of simple structure, high sensitivity, and compact size [1,2]. Since air cavities created in the fiber have a small thermal expansion coefficient, in-fiber air-cavity-based FPIs have been used to develop temperature-insensitive sensors for measuring refractive index (RI) [3–5], tensile strain [6–13], and pressure [14,15]. Unfortunately, it is difficult or impossible to create directly an air cavity in the fiber, so that complicated pretreatments have to been done to achieve in-fiber air-cavity-based FPIs. For example, air cavities were achieved during splicing two cleaved fiber ends by use of femtosecond laser micromaching [5,6,16] and chemical etching [11,13] to create a microhole on the fiber end in advance. In addition, in-fiber FPIs with an air cavity were demonstrated by employing special optical-fiber structures, such as hollow-core photonic crystal fibers (PCFs) [4,7], solid-core PCFs [8,10], and silica capillaries [14]. However, all these techniques above require complicated pretreatments, expensive PCFs, and/or other special optical fibers.

In this Letter, we demonstrated a promising technique to create an air-cavity-based FPI by means of splicing together two sections of standard single-mode fibers (SMFs), accompanying easy pretreatment on the fiber ends. Such an FPI could be used to develop a high-sensitivity strain sensor with a low cross sensitivity between temperature and tensile stain. And the sensitivity of the strain sensor can be enhanced to 6.0 pm/με by means of reshaping an air cavity created in the fiber.

Figure 1 illustrates the fabrication process of an in-fiber air-cavity-based FPI. First of all, an end of a standard SMF (Corning SMF-28) was immersed into a commercial RI matching liquid (Cargille Labs, http://www.cargille.com) to coat a liquid film on the end surface. Such two sections of SMFs with liquid-coated ends were placed in the left and right fiber holders, respectively, of a commercial fusion splicer (Fujikura FSM-60S), as shown in Fig. 1(I). Before being immersed into the liquid, the fiber end was reshaped into hemispherical and smooth ends by means of electrical arc discharge in order to enlarge the surface of the fiber ends and to coat much liquid on the fiber ends. Second, the left and right fiber ends were moved toward each other until an overlap of $2d$ was achieved at the touching region of the two fiber ends via the left and right motors of the fusion splicer, as shown in Fig. 1(II), where d_l and d_r show the moved distance of the left and right fiber ends, respectively, before the two fiber ends are touched with each other, and d shows the moved distance of each fiber end after the two fiber ends touch each other. Third, arc discharge was done with default parameters for splicing a standard SMF in the fusion splicer. Consequently, two fiber ends were spliced with each other, and an air bubble was created in the spliced joint, as shown in Figs. 1(III) and 2(a), resulting from the evaporation of the liquid coated on the fiber end facet and quick vaporization and freeze of silica material during arc discharge. Note that (1) the manual operation mode of the fusion splicer (FSM-60S) was used to fabricate the in-fiber air cavity samples; (2) three types of discharge parameters, i.e., ARC1, ARC2, and REARC, are available in the operation menu of the splicer; (3) only the discharge parameter of ARC1 was employed during our pretreating of the fiber ends, fabricating air cavity samples, and reshaping

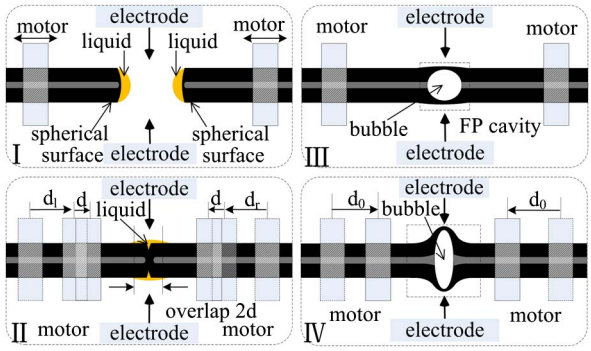

Fig. 1. Schematic diagrams of fabrication process of in-fiber FPI based on an air bubble.

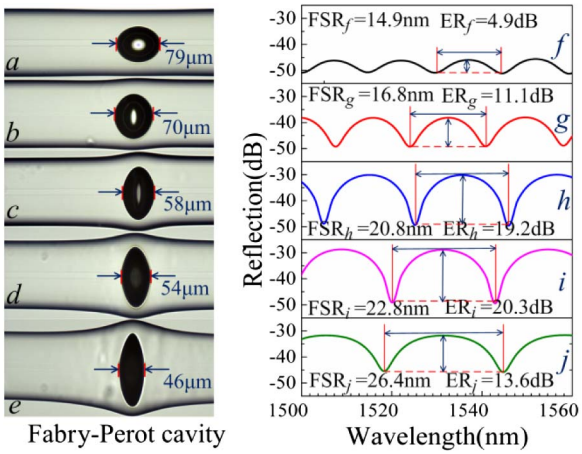

Fig. 2. (a), (b), (c), (d), and (e) Microscope images of the created air bubble with a cavity length of 79, 70, 58, 54, and 46 μm, respectively; (f)–(j) the corresponding reflection spectra of the air-cavity-based FPI. FSR, free spectra range; ER, extinction ratio.

the air cavities. Such an in-fiber air bubble/cavity could be used to develop a promising fiber-optic FPI. As shown in Fig. 2, an interference pattern was observed in the reflection spectrum of the air-cavity-based FPI by use of a 3 dB coupler, a broadband light source (ASE-LIGHGSOURCE), and an optical spectrum analyzer (OSA, YOKOGAWA AQ6370C).

Our experiments show that the diameter of the created air bubble depends strongly on the overlap of $2d$ and the viscosity of the coated liquid. Providing other fabrication parameters are not changed; the more overlap of $2d$ is applied to the spliced joint, a larger air bubble can be achieved. Compared with complicated pretreatments, e.g., femtosecond laser micromaching for creating a microhole on the fiber end [5,6], we demonstrated an easy pretreatment, e.g., coating a liquid film on the fiber end, to create an air bubble in the spliced joint. The intensity of the interference fringe in the reflection spectrum can be given by

$$I = I_1 + I_2 + 2\sqrt{I_1 I_2}\cos(\gamma), \tag{1}$$

where I_1 and I_2 are the intensities of light reflected at the two cavity interfaces, respectively, and γ is the phase different shift between the two reflected lights. Free spectral range of the interference fringes of the air-cavity-based FPI can be given by

$$\mathrm{FSR} = \lambda^2/(2nL_B), \tag{2}$$

where λ is the wavelength of light, n is the RI of the medium, i.e., air, trapped inside the bubble, and L_B is the cavity length of the air bubble created in the spliced joint.

The in-fiber air bubble illustrated in Fig. 2 can be reshaped to enhance the extinction ratio of the interference fringe and change the FSR by means of repeating arc discharges, as discussed below. As shown in Fig. 1(IV), the left and right fiber holders were moved again toward each other by a distance of d_0 in order to apply an axial pressure to the spliced joint, and then arc discharge was done again. Consequently, the spherical air bubble was reshaped into an elliptical one with a shorter cavity length along the fiber axis. Repeating the process above, we achieved a series of elliptical air bubbles with different cavity lengths of 79, 70, 58, 54, and 46 μm by means of applying different overlap of $2d_0$ during repeated arc discharges, as shown in Figs. 2(a)–2(e). The corresponding reflection spectra of the air-cavity-based FPIs are illustrated in Figs. 2(f)–2(j), respectively, in which the FSR of the interference fringes is 14.9, 16.8, 20.8, 22.8, and 26.4 nm, respectively, and the extinction ratio is 4.9, 11.1, 19.2, 20.3, and 13.5 dB, respectively. It can be found from Fig. 2 that, with the decrease of the cavity length from 79 to 46 μm, the FSR around 1530 nm is increased from 14.9 to 26.4 nm, and the extinction ratio is enhanced from 4.9 to 20.3 dB and is reduced to 13.5 dB. This is due to the fact that the reshape of the air bubble changes the intensity of light reflected on the air cavity wall. We measured the insertion loss of the air bubble with a cavity length of 79, 70, 58, 54, and 46 μm by means of testing its transmission spectra within the wavelength range from 1450 to 1600 nm. As shown in Fig. 3, the insertion loss reduces with the decrease of the cavity length, and the air bubble with a cavity length of 46 μm has an insertion loss of about 6.5 dB at the wavelength of 1550 nm. According to Eq. (2), we also calculated the FSR around 1530 nm. As shown in Fig. 4, the measured cavity lengths of the air bubble agree well with the calculated results.

We investigated the responses of the air-cavity-based FPI samples with different cavity lengths to the applied tensile strain. First, one end of the air-cavity-based FPI with a cavity length of 79 μm, as illustrated in Fig. 2(a), was fixed, and another end was attached to a translation stage with a resolution of 10 μm. The total length of the stretched fiber, including the SMF and the air bubble, was 400 mm. The wavelength shift of the interference fringe around 1545 nm was measured while the tensile strain was increased from 0 to 1050 με with a step of 50 με. Second, the air bubble with a cavity length of 79 μm was reshaped to shorten its cavity length to 70 μm by use of the arc discharge technique illustrated in Figs. 1(IV) and 2(b). And then the response of the air-cavity-based FPI with a cavity length of 70 μm to the applied tensile strain was investigated. The experiment

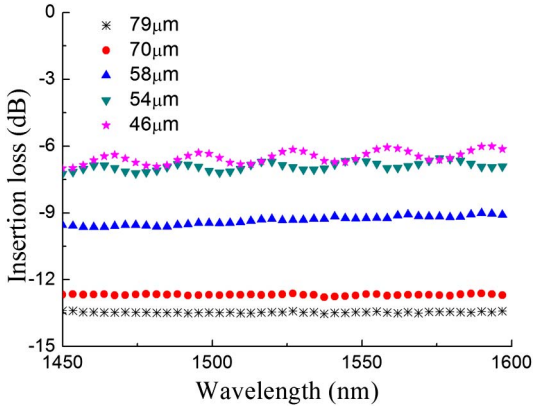

Fig. 3. Insertion loss of the air bubble with a cavity length of 79, 70, 58, 54, and 46 μm.

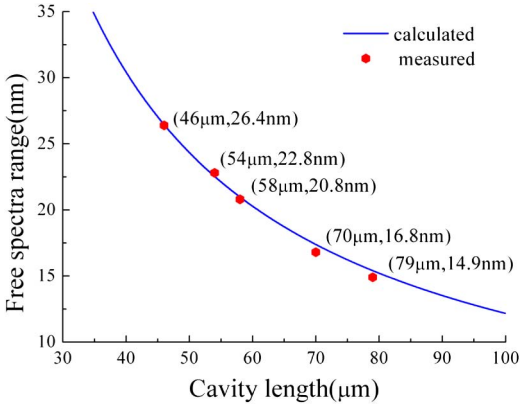

Fig. 4. Measured and calculated FSR of interference fringes of the in-fiber air-cavity-based FPI with different cavity lengths of 46, 54, 58, 70, and 79 μm.

process above was repeated until the response of the air-cavity-based FPI samples with a cavity length of 58, 54, and 46 μm, as illustrated in Figs. 2(c)–2(e), to the applied tensile strain was investigated. As shown in Figs. 5(a) and 5(b), the dip wavelength of the interference fringe of each air-cavity-based FPI sample shifts linearly toward a longer wavelength with the increased tensile strain. And the shorter cavity length the FPI sample has, a higher

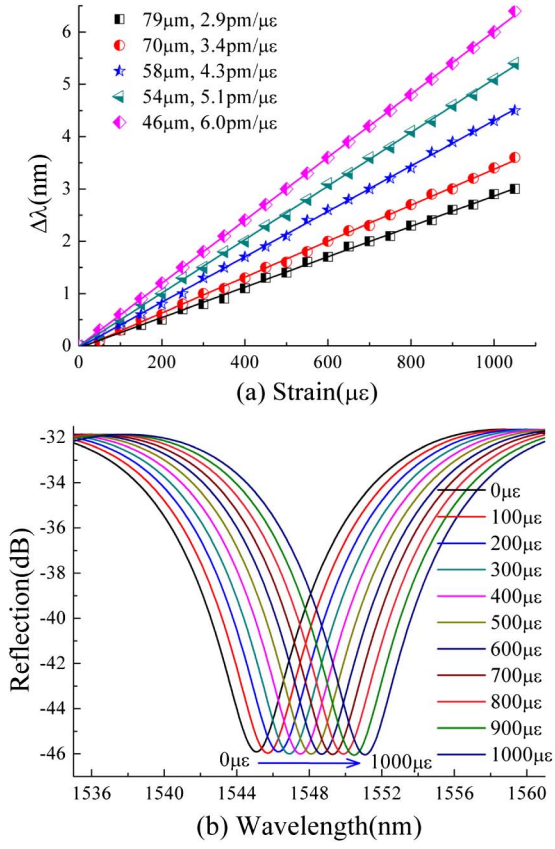

Fig. 5. (a) Wavelength shift of the interference fringe around 1545 nm as a function of tensile strain applied to the air-cavity-based FPI sample with different cavity length of (◨) 79 μm, (◐) 70 μm, (★) 58 μm, (◀) 54 μm, and (◆) 46 μm. (b) Reflection spectrum evolution of the air-cavity-based FPI sample with a cavity length of 46 μm while the tensile strain increases from 0 to 1000 με.

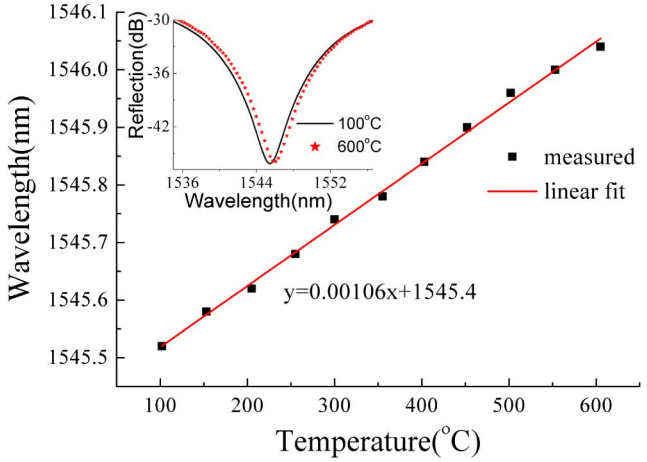

Fig. 6. Temperature response of the dip wavelength in the reflection spectrum of the air-cavity-based FPI sample with a cavity length of 46 μm.

strain sensitivity the wavelength is. Hence the strain sensitivity of the air-cavity-based FPI sensor can be enhanced by means of reshaping the air bubble to shorten the cavity length via arc-discharge technique. For example, the strain sensitivity of the air-cavity-based FPI was enhanced from 2.9 to 6.0 pm/με while the cavity length was shorten from 79 to 46 μm, as shown in Fig. 5(a). Providing an optical spectrum analyzer (YOKOGAWA AQ6370C) with a resolution of 0.02 nm is employed, a strain resolution of 3.3 με can be achieved in the application of our proposed strain sensor based on Fabry–Perot interference.

We also investigated the temperature responses of the air-cavity-based FPI sample with a cavity length of 46 μm. The FPI sample was placed in a tube furnace to raise its temperature from 100°C to 600°C with a step of 50°C. As shown in Fig. 6, the dip wavelength in the reflection spectrum the FPI sample was shifted toward a longer wavelength with a low temperature sensitivity of only 1.1 pm/°C. In other words, the interference fringe is insensitive to temperature [17]. According to the strain and temperature sensitivity of the interference fringe, in case no temperature compensation is done, the temperature-induced strain measurement error is less than 0.2 με/°C. Therefore, the FPI-based strain sensor effectively reduces the cross sensitivity between strain and temperature.

In summary, we demonstrated a versatile technique for fabricating a micro air bubble in the fiber. The air bubble can be reshaped to change its cavity length by arc-discharge technique. Such an in-fiber air bubble can be used to develop a high-sensitivity strain sensor based on Fabry–Perot interference. The sensitivity of this strain sensor was enhanced to 6.0 pm/με by improving the cavity length of the FPI. Moreover, such a strain sensor reduces the cross sensitivity between tensile strain and temperature.

This work was supported by the National Natural Science Foundation of China (grant nos. 11174064, 61308027, and 61377090), the Science & Technology Innovation Commission of Shenzhen (grant nos. KQCX20120815161444632 and JCYJ20130329140017

262), and the Distinguished Professors Funding from Shenzhen University and Guangdong Province Pearl River Scholars.

References

1. T. Zhu, D. Wu, M. Liu, and D. W. Duan, Sensors **12**, 10430 (2012).
2. B. H. Lee, Y. H. Kim, K. S. Park, J. B. Eom, M. J. Kim, B. S. Rho, and H. Y. Choi, Sensors **12**, 2467 (2012).
3. Y. Wang, D. Wang, C. Liao, T. Hu, J. Guo, and H. Wei, Opt. Lett. **38**, 269 (2013).
4. D. Jáuregui Vázquez, J. M. Estudillo Ayala, R. Rojas Laguna, E. Vargas Rodríguez, J. M. Sierra Hernández, J. C. Hernández García, and R. I. Mata Chávez, Sensors **13**, 6355 (2013).
5. C. Liao, T. Hu, and D. Wang, Opt. Express **20**, 22813 (2012).
6. C. Liao, D. Wang, and Y. Wang, Opt. Lett. **38**, 757 (2013).
7. M. S. Ferreira, J. Bierlich, J. Kobelke, K. Schuster, J. L. Santos, and O. Frazao, Opt. Express **20**, 21946 (2012).
8. F. Favero, L. Araujo, G. Bouwmans, V. Finazzi, J. Villatoro, and V. Pruneri, Opt. Express **20**, 7112 (2012).
9. D.-W. Duan, Y.-j. Rao, Y.-S. Hou, and T. Zhu, Appl. Opt. **51**, 1033 (2012).
10. J. Villatoro, V. Finazzi, G. Coviello, and V. Pruneri, Opt. Lett. **34**, 2441 (2009).
11. E. Cibula and D. Donlagic, Opt. Express **15**, 8719 (2007).
12. Y. P. Wang, D. Wang, W. Jin, and X. H. Fang, IEEE J. Quantum Electron. **42**, 868 (2006).
13. X. Chen, F. Shen, Z. Wang, Z. Huang, and A. Wang, Appl. Opt. **45**, 7760 (2006).
14. Y. Wang, D. Wang, C. Wang, and T. Hu, Opt. Express **21**, 14084 (2013).
15. J. Ma, J. Ju, L. Jin, and W. Jin, IEEE Photon. Technol. Lett. **23**, 1561 (2011).
16. C. Liao, L. Xu, C. Wang, D. N. Wang, Y. Wang, Q. Wang, K. Yang, Z. Li, X. Zhong, J. Zhou, and Y. Liu, Opt. Lett. **38**, 4473 (2013).
17. Y. Wang, W. Jin, and D. Wang, Opt. Lasers Eng. **47**, 1044 (2009).